ARTICLE

Room-temperature in-plane thermoelectric transport in 2H-$MoTe_2$ with back-gate bias modulation

Received 00th January 20xx,
Accepted 00th January 20xx

DOI: 10.1039/x0xx00000x

Tianhui Zhu, [#a] Sree Sourav Das,[a] Safoura Nayebsadeghi,[b] Sergiy Krylyuk,[c] Costel Constantin,[d] Keivan Esfarjani[b,e,f], Albert V. Davydov,[c] and Mona Zebarjadi*[a,e]

On-chip integrated nanoscale coolers are in high demand due to the shrinking device size of modern electronics. Thermoelectric and thermionic coolers made out of 2D layered materials are one attractive solution. 2D transition metal dichalcogenides can have relatively good electrical properties and relatively low thermal conductivities, which indicates their potential to reach a high thermoelectric figure of merit. Here, we report a comprehensive experimental and theoretical study on the thermoelectric transport properties of thin 2H-$MoTe_2$ flakes prepared in field-effect transistor geometry to enable electrostatic gating. The electrical conductivity and the Seebeck coefficient were measured as a function of the back gate voltage. Applying the back gate voltage was found to enhance the thermoelectric power factor by up to 45 % compared to the zero-bias value. The in-plane thermal conductivity of 9.8 ± 3.7 $Wm^{-1}K^{-1}$ was measured using the heat diffusion imaging method in a 25 nm thick flake. The electronic band structure and the electrical transport are further studied using first-principles calculations with energy-dependent relaxation times, by considering electron-phonon scattering and ionized impurity scattering. First-principles calculations are also performed to obtain thermal conductivity values using both the relaxation time approximation and the full iterative solution to the phonon Boltzmann equation, as a validation of the experimental measurements. This fundamental study of 2H-$MoTe_2$ expands our understanding of the 2D thermoelectrics and offers pathways to further enhancements in the device's performance.

Introduction

In recent years, there has been growing research interest in 2D thermoelectric materials.[1] Thermoelectric modules can convert thermal energy to electricity or use electricity for heat management. The thermoelectric power factor is defined as $PF = \sigma S^2$, where σ is the electrical conductivity and S is the Seebeck coefficient, $S = -\frac{\Delta V}{\Delta T}$. Seebeck effect describes how much voltage difference (ΔV) can be generated with a temperature difference (ΔT) and is the basis of thermoelectric power generation. Power factor times temperature (*PFT*) is also often used since it shares the same unit as thermal conductivity, k. The efficiency of thermoelectric energy conversion is an increasing function of the thermoelectric figure of merit, $ZT = \frac{PFT}{k}$.

With the continued miniaturization of modern electronics, the dissipated power density keeps increasing[2]. 2D materials are great candidates for nanoscale power generation to recycle waste heat and for hot spot cooling due to their nanometer thicknesses. They often possess unique chemical, mechanical, and physical properties compared to their bulk counterparts[3,4]. As a result of the small thickness, the Fermi level and the charge carrier concentrations of 2D materials can be tuned by electrostatic gating using the electric field effect[5]. This is an advantage over bulk materials as it avoids chemical doping processes and allows real-time Fermi-level tuning and optimization of the thermoelectric figure of merit using a single sample. For example, monolayer graphene on hexagonal boron nitride (hBN) has been shown to have a *PFT* as high as 10.35 $Wm^{-1}K^{-1}$ at room temperature under the optimal back gate bias[6], which is one order of magnitude higher than that of commercial thermoelectric material, bulk Bi_2Te_3. Graphene also has a high thermal conductivity on the order of 1000 $Wm^{-1}K^{-1}$. While this makes graphene an excellent candidate for active cooling purposes[7–9], where passive cooling by phonon transport works together with active cooling by the Peltier effect to conduct heat away from the hot spots, it also means that its *ZT* is not as appealing for thermoelectric energy conversion applications.

For conventional energy conversion applications, we turn to 2D transition metal dichalcogenides (TMDs). They possess a

[a.] *Department of Electrical and Computer Engineering, University of Virginia, Charlottesville, Virginia, 22904, United States*
[b.] *Department of Mechanical and Aerospace Engineering, University of Virginia Charlottesville, Virginia, 22904, United States,*
[c.] *Materials Science and Engineering Division, National Institute of Standards and Technology, Gaithersburg, Maryland, 20899, United States.*
[d.] *Department of Physics and Astronomy, James Madison University, Harrisonburg, Virginia, 22807, USA.*
[e.] *Department of Materials Science and Engineering, University of Virginia, Charlottesville, Virginia, 22904, United States*
[f.] *Department of Physics, University of Virginia, Charlottesville, Virginia, 22904, United States*
#Present address: Department of Physics, University of California, Santa Cruz, California, 95064, USA
*Author to who correspondence should be addressed: m.zebarjadi@virginia.edu
† Electronic Supplementary Information (ESI) available. See DOI: 10.1039/x0xx00000x

wide range of tunable electronic properties (from insulating to superconducting) and a relatively low thermal conductivity (much smaller than graphene), which may result in high *ZT* values. High *ZT* requires a large Seebeck coefficient, high electrical conductivity, and low thermal conductivity. At the same time, the interplay between these transport parameters means that *ZT* enhancement is complex: for example, the higher carrier concentration is beneficial for higher electrical conductivity but leads to lower Seebeck coefficient values. The intricate balance usually occurs in highly doped semiconductors[10] or possibly semimetals[11].

2D semiconductor MoS_2 has been studied extensively for thermoelectric applications and the best-performing samples showed a *PFT* close to 2.5 $Wm^{-1}K^{-1}$ with high mobility of 60 $cm^2V^{-1}s^{-1}$ (bilayer on SiO_2 at room temperature)[12] and up to 350 $cm^2V^{-1}s^{-1}$ (six layers on hBN at 50 K)[13]. This large *PFT* has been achieved following years of continued research effort. In 2014, a large Seebeck coefficient of −30 mV/K was reported for CVD-grown monolayer MoS_2; the power factor, however, was small due to low conductance.[14] Two years after this, bilayer MoS_2 was shown to have a Seebeck coefficient of –450 μV/K and a power factor of 1.5 $Wm^{-1}K^{-1}$.[15] Characterization of the in-plane thermal conductivity of many 2D materials is challenging due to their small sample dimensions. In the case of MoS_2, there have been large discrepancies depending on the sample qualities and the experimental techniques. Even with the same Raman spectroscopy-based technique, reported values were between 35 and 85 $Wm^{-1}K^{-1}$ for monolayer MoS_2 [16–19], where the sample absorption coefficient and the sample quality were expected to play a significant role. The thermal bridge method had a thermal conductivity of few-layer MoS_2 at about 45 $Wm^{-1}K^{-1}$ [20] and monolayer MoS_2 at 24 $Wm^{-1}K^{-1}$ [21]. Molecular dynamics calculations revealed thermal conductivity of 117 $Wm^{-1}K^{-1}$ for suspended monolayers and 31 $Wm^{-1}K^{-1}$ for supported samples.[22] As sample quality also affects carrier mobility and transport performance, these large uncertainties make it less plausible to estimate *ZT* by combining *PFT* and *k* across different studies.

2H-$MoTe_2$ is another semiconducting molybdenum-based TMD material with an indirect gap of 0.83 eV in the bulk form and a direct gap of 1.1 eV in the monolayer limit.[23,24] Most of the research on $MoTe_2$ has been focused on electronic[25–28] and optoelectronic[26,29] applications whereas the studies of its thermoelectric properties are limited. Seebeck coefficient of n-type single crystal bulk $MoTe_2$ was measured to be around –400 μV/K from 77 K to 300 K[30]. At room temperature, its electrical conductivity was about 750 S/m and its *PFT* was 0.036 $Wm^{-1}K^{-1}$.[30] A 330 nm thick 2H-$MoTe_2$ thin film prepared by magnetron co-sputtering showed a p-n type transition with increasing temperature, giving a maximum *PFT* of 0.15 $Wm^{-1}K^{-1}$ at 460 K for p-type conduction and 0.55 $Wm^{-1}K^{-1}$ at 670 K for n-type conduction[31]. At room temperatures, the sample was p-type with $\sigma = 1.5 \times 10^4$ S/m, $S = 25$ μV/K and a *PFT* of 0.0028 $Wm^{-1}K^{-1}$.[31] The enhancement in *PFT* at higher temperature was a result of increased Seebeck coefficient values with increasing conductivity, which was unusual and was attributed to improved mobility. Investigations of the thermal conductivity of $MoTe_2$ are also very limited. Yan et al. determined the c-axis thermal conductivity of $MoTe_2$ as 1.5 $Wm^{-1}K^{-1}$ at 300 K using time-domain thermoreflectance (TDTR) method.[32] DFT calculations estimated the in-plane lattice thermal conductivity of monolayer $MoTe_2$ to be around 60 $Wm^{-1}K^{-1}$ at room temperature.[33] These studies indicate that 2H-$MoTe_2$ can be a potential candidate for thermoelectrics, especially in the few-layer limit when the band structure changes due to quantum confinement and the chemical potential can be tuned by the gate voltage.

In this manuscript, we report a comprehensive experimental and theoretical study of room-temperature in-plane thermoelectric transport in thin 2H-$MoTe_2$ flakes. Electrical conductivity and Seebeck coefficient are measured as a function of the back gate bias. Further understanding of the electrical transport data is provided by first-principles calculations with energy-dependent relaxation times, by considering electron-phonon scattering and ionized impurity scattering. Thermal conductivity is also reported, which, to the best of our knowledge, is the first in-plane thermal transport characterization of thin $MoTe_2$. Due to the difficulty in measuring the thermal conductivity of thin 2D films, most of the literature reports only the power factor. The thermal conductivity measurements enable us to estimate *ZT* as well as to provide a more complete evaluation of the $MoTe_2$ material in terms of thermoelectric applications. In-plane thermal conductivity of bulk MoTe2 is also calculated within both the relaxation time approximation and the full iterative solution to the phonon Boltzmann equation, and compared to the experimental data.

Materials and Methods

$MoTe_2$ crystals were grown by the Chemical Vapor Transport (CVT) method using polycrystalline $MoTe_2$ charge and iodine transport agent. The growth was conducted in a vacuum-sealed quartz ampoule at 970 °C for 7 d followed by a 3 d annealing at 800 °C to stabilize the hexagonal 2H phase. Phase purity was confirmed by powder X-ray diffraction measurements.

Device fabrication

Thin 2H-$MoTe_2$ flakes were exfoliated onto 300 nm SiO_2/p^+-Si substrates by the Scotch tape method. The substrates were pre-cleaned by acetone and isopropanol sonication, followed by annealing at 400 °C in forming gas (5% H_2/95% Ar) to remove chemical residues. Flakes with a uniform thickness were chosen under an optical microscope. The thickness of the exfoliated flakes was characterized by a Bruker Dimension Icon atomic force microscope (AFM) and was around 25 nm for the two devices presented below. The standard thermoelectric electrode patterns were prepared using laser lithography (385 nm), which includes one heater, two thermometers, and two side contacts, see inset in Fig. 1 for the geometry of the device. 5 nm Ti and 100 nm Au were evaporated as contact metals (base pressure < 10^{-5} Torr, 1 Å/s). The shape of each flake was identified under a microscope and subsequently etched to a rectangular shape by opening etch windows with

laser lithography and then reactive ion etching (RIE) with SF_6 (30 W) for up to 1 min. Exposure to air during the fabrication process might cause some surface oxidation, but the oxidation is known only to occur in the top two or three layers near the surface and the bulk of the flake remains intact[34]. The samples were kept inside an argon-filled glovebox and annealed in a high vacuum (~ 10^{-6} Torr) at 325 °C for 30 min in the cryostat immediately before measurements to minimize effects from environmental contamination.

Measurement setup

The electrical transport measurements were performed in a JANIS cryostat system customized for transport measurements in a high vacuum (~ 10^{-6} Torr). A Keithley 2401 SourceMeter was used to measure the four-probe resistance under 1 μA current. Back gate voltage, V_g, was applied to the highly doped Si substrate using a Keithley 2400 SourceMeter. The leakage current from the back gate was limited to a few nA for V_g up to 100 V. Up to 30 mA current was passed through the heater during Seebeck coefficient measurements and the generated Seebeck voltage was recorded by a Keithley 2182A nanovoltmeter.

The thermal conductivity was measured following the heat diffusion imaging method.[35] This thermoreflectance-based approach captures the temperature decay along the sample after heat flow injection and extracts the thermal conductivity using the heat spreader model. The thermoreflectance imaging system from Microsanj LLC used a 532 nm green LED as the light source. Electrical pulses (5 V, 5 ms) were sent to the heater.

First-principles calculations

First-principles calculations were performed using the density functional theory (DFT) and density functional perturbation theory (DFPT) as implemented in the QUANTUM ESPRESSO package. [36] We used ultrasoft pseudopotential[37] with modified Perdew-Burke-Ernzerhof generalized gradient approximation (PBEsol)[38]. A kinetic energy cutoff of 70 Ry and Monkhorst-Pack k-point mesh of $10\times10\times4$ was employed in the electronic structure calculation. The convergence threshold of energy was set to 10^{-7} in the self-consistent calculation. The lattice parameters of hexagonal $MoTe_2$ were chosen based on experimental results.[39] The dynamical matrix was computed on a 4×4×2 q-point mesh in the phonon calculations and later interpolated by Fourier transform to compute the phonon modes and frequencies at other general k-points. To accurately describe the thermoelectric properties, we considered the energy-dependent relaxation times including electron-phonon and ionized impurity scattering in transport calculations. The electron-phonon lifetime (τ_{e-ph}) were calculated using the PERTURBO package[40] and the ionized impurity scattering rates were computed using a modified Brooks-Herring approach for strongly screened potential[41]. PERTURBO utilizes the Wannier interpolation scheme [42,43] and interpolates the electron-phonon coupling matrix from a coarse grid to a fine grid (60×60×60). Wannierization of a total of 24 bands was performed using projections of d_{xy}, d_{xz}, d_{yz}, d_{z2}, d_{x2-y2} orbitals on each Mo atom and p_x, p_y, p_z orbitals on each Se atom. Later, the ionized impurity scattering was calculated using the following equation [41] and added with the electron-phonon scattering to get the total relaxation time:

$$\frac{1}{\tau_{ion}} = \frac{\pi(N_I/Z)}{\hbar}\left(\frac{q^2 L_D^2}{\varepsilon_0 \varepsilon_r}\right)^2 g(E), \qquad (1)$$

where $g(E)$ is the density of states, $\hbar$ is the reduced Plank constant, ε_r is the relative permittivity, ε_0 is the permittivity of free space, N_I is the impurity carrier concentration, q is the electronic charge, and Z is the charge of the vacancy/impurity atoms. Here, n-type behavior in $MoTe_2$ is attributed to tellurium (Te) vacancies[44]. Tellurium vacancy results in the average of 2 conduction electrons per vacancy and therefore, $Z = 2$ is used for the calculation of ionized impurity scattering rates of undoped $MoTe_2$ sample. L_D is the screening length and is given by:

$$\frac{1}{L_D^2} = \frac{q^2}{\varepsilon}\int g(E)\frac{\partial f}{\partial E}dE, \qquad (2)$$

where f is the Fermi-Dirac distribution function.

Finally, electronic transport calculation was performed in PERTURBO based on the semi-classical Boltzmann transport method with energy-dependent total relaxation times. For comparison, the transport properties were also evaluated using BoltzTraP package[45] with constant relaxation time approximation (CRTA)[46]. The transport calculations were performed in the in-plane directions and so, van der Waals interactions were not considered in the DFT and DFPT calculations. Using a similar approach, recently we have reproduced thermoelectric transport properties of $MoSe_2$[47] and $SnSe_2$.[48]

In the case of phonons, we performed first-principles calculations by using the Vienna ab initio simulation (VASP), SCAN-rVV10 XC potential to calculate the harmonic and anharmonic interatomic force constants using a $4\times4\times2$ supercell. The thermal conductivity of naturally occurring isotopic and hypothetical isotopically pure $MoTe_2$ bulk were then calculated on a converged q-space grid $16\times16\times4$ by iteratively solving the phonon Boltzmann transport equation as implemented in the Sheng-BTE package.

Results and Discussion

Electrical transport characterization

The electrical conductivity of the thin $MoTe_2$ sample is plotted in Fig. 1(a) as a function of V_g. Without the application of the back gate voltage, the value was around 1350 S/m. The conductivity of $MoTe_2$ reported in the literature varies depending on the sample preparation. The observed electrical conductivity is within the reported literature values.[30,31] In comparison to the samples from the two references, the electrical conductivity of our sample doubles that of the bulk $MoTe_2$ crystal[30] while it is one order of magnitude smaller than that of the sputtered thin film sample[31]. As V_g is swept from −80 V to 80 V, its electrical conductivity varies by one order of magnitude, from 250 S/m to 2550 S/m. The conductivity goes up with increasing gate voltages. Since V_g is connected to the highly doped Si, increasing V_g means increasing electron density in the sample and thus the sample exhibits n-type behavior.

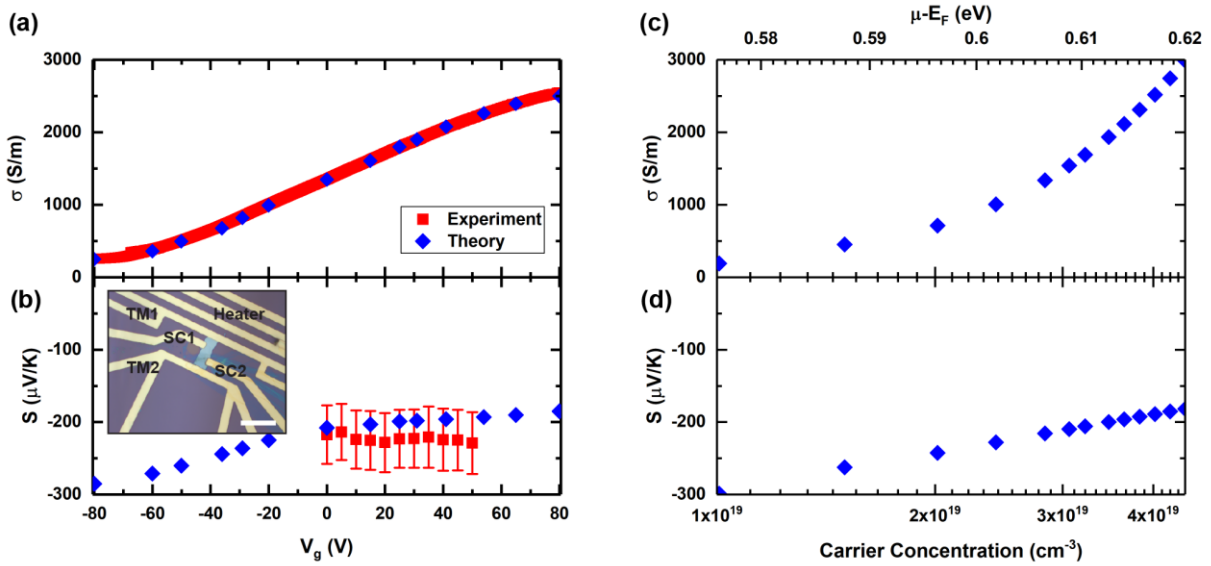

Fig. 1 Experimental (a) electrical conductivity and (b) Seebeck coefficient of the exfoliated thin $MoTe_2$ sample as a function of the gate voltage, compared with theoretically obtained values. Calculated (c) electrical conductivity and (d) Seebeck coefficients as a function of the carrier concentration (bottom axis) and the chemical potential with respect to the intrinsic Fermi level, μ–E_F (top axis). The inset in (c) shows an optical image of the device, with the heater, the thermometers (TMs) and the side contacts (SC) noted. The scale bar is 20 μm.

Another thicker sample of 100 nm was also measured and exhibited similar conductivity values and similar trends as a function of V_g. The results were included in ESI. The Seebeck coefficient was measured at different V_g as shown in Fig. 1(b). The negative S value confirms the n-type conduction of the sample. At V_g = 0 V, the sample shows a Seebeck coefficient of −210 μV/K. This room temperature value is about half of that of the bulk single crystal[30] but one order of magnitude larger than that of the sputtered thin film[31]. The Seebeck voltage detection was noisy in the entire measurement range that prevented reliable measurements at negative V_g. Moreover, at large negative Vg values, an offset open voltage was detected even when the heater was turned off, which should have been close to zero. Similar behavior has been observed and explained for MoS_2: when the semiconductor channel resistance becomes too high, resistive coupling from the back gate to the channel causes the offset voltage.[15] The input bias current up to 120 pA from the nanovoltmeter also contributes to the offset voltage and the noise, which was observed for MoS_2[15] and for Si metal-oxide-semiconductor FETs with high resistance[49]. Presumably due to the noisy signals, no significant change in the Seebeck coefficient was observed within the V_g = 0—50 V range, although one could expect a lower Seebeck coefficient with higher electrical conductivity. The expected change in S value against V_g was calculated theoretically in the following section and is shown to be within our experimental error bars. The theoretical Seebeck coefficient reduces to −185 μV/K at V_g = 80 V and grows to −285 μV/K at V_g = −80 V (Fig. 1(b)).

Electronic Transport calculations

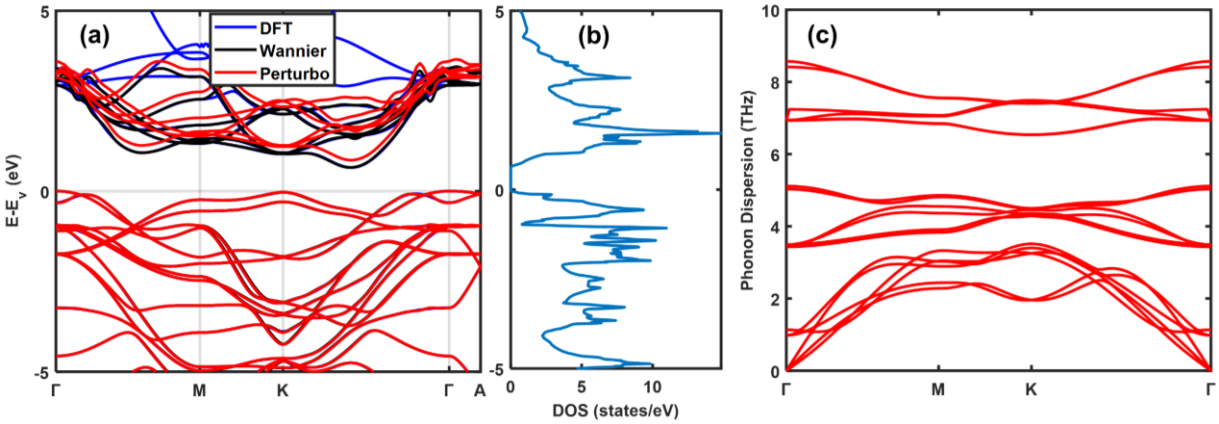

Fig. 2 (a) Electronic band structure, (b) electronic DOS from DFT, and (c) phonon dispersion of bulk $MoTe_2$.

Since the devices are over 10 layers thick, they are considered bulk in the band structure calculations. Electronic band structure, electronic density of states (DOS), and phonon-dispersion of bulk $MoTe_2$ are shown in Fig. 2. The obtained DFT band structure is in good agreement with previous calculations[50,51] and Wannier interpolated band structure. The top of the valence band is at Γ, and the bottom of the conduction band is halfway between Γ-K, resulting in an indirect gap of 0.66 eV. It is well known that PBE functionals underestimate the bandgap for most insulators and semiconductors. So, we shifted the conduction bands during Wannier to PERTURBO interpolation and obtained a band gap of 0.87 eV which closely matches the experimental gap of 0.83 eV[26,27,52].

The phonon dispersion of $MoTe_2$ is shown in Fig. 2(c). As the unit cell of hexagonal $MoTe_2$ has 6 atoms, there are 18 phonon modes at each k-point. Our results are in agreement with other DFPT calculations[53].

The Seebeck coefficient and electrical conductivity at room temperature are evaluated using semi-classical BTE including electron-phonon scattering and ionized impurity scattering in PERTRUBO. The ionized impurity scattering rates are calculated using a modified Brooks-Herring approach and added with electron-phonon scattering using the Matthiessen rule. Both scattering rates are shown in Fig. 3 along with the electronic DOS. It is evident that total scattering times are dominated by the ionized impurity scattering. Finally, transport calculations are performed considering energy-dependent total scattering times. At first, we used carrier concentration as a fitting parameter to match the experimental electrical conductivities at different gate voltages and reported the corresponding Seebeck coefficients. We found that the obtained Seebeck coefficients are within the error bar of the experimentally reported values in Fig. 1(b). Figure 1 (c, d) also show the raw theoretical calculations with no fitting of conductivity and Seebeck coefficient as a function of chemical potential and carrier concentration (1×10^{19} cm^{-3} to 4×10^{19} cm^{-3}), respectively. At zero gate voltage, experimental electrical conductivity and Seebeck are around 1350 S/m and -210 μV/K, respectively, which are corresponding to the carrier concentration of 2.9×10^{19} cm^{-3} and chemical potential of 0.6 eV above the intrinsic Fermi level (E_F) as shown in Fig. 1(c, d). With increasing gate voltages, electrical conductivity and Seebeck coefficient follow opposite trends: as the carrier concentration increases with the increasing gate voltage, the Seebeck coefficient decreases and the electrical conductivity increases. The Seebeck coefficient changes from -300 μV/K at 1×10^{19} cm^{-3} to −189 μV/K at 4×10^{19} cm^{-3}. It can be seen that the experimental values are within the range of predicted theoretical values.

We have also analyzed the effects of electron-phonon and ionized impurity scattering on transport properties. The inclusion of ionized impurity scattering does not have any significant effect on the Seebeck coefficient, because the Seebeck coefficient is not sensitive to the details of relaxation times as shown in first principles-based calculations. However, with the ionized impurity scattering included, the electrical conductivity closely matches the experimental results. After successfully modeling the experimental Seebeck coefficient and electrical conductivity within energy-dependent relaxation time, we compared the results obtained from energy-dependent relaxation time and CRTA[54] as shown in Table 1. The details of the Seebeck coefficient and electrical conductivity obtained from BoltzTraP[45] are discussed in ESI Fig. S2. Within CRTA, relaxation times are assumed to be energy and momentum independent and the same constant for all electrons. As implemented in BoltzTraP, the constant relaxation time is not calculated. Hence, we take the average electron-phonon and ionized impurity scattering rates weighted by df/dE calculated within the Fermi-window $(\mu \pm 20K_BT)$ as the constant and use it in the CRTA calculations. This relaxation time at room temperature and at zero gate is 0.94 fs. Using this value, the obtained electrical conductivity is 2018 S/m and the Seebeck coefficient is -255 μV/K. The discrepancies in the results between PERTURBO and BoltzTraP come from the use of different relaxation times. To accurately describe the transport properties of a material, energy or momentum dependent scattering times need to be considered.

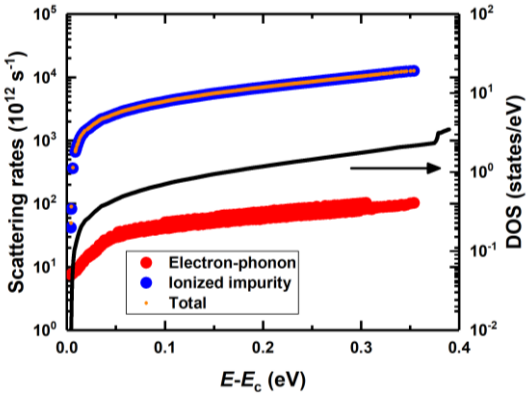

Fig. 3 Scattering rates and DOS as a function of the energy relative to the conduction band minimum (E_C).

Table 1. Comparison between experimental data at V_g = 0 and theoretical calculations under different conditions

Parameters		***S* (μV/K)**	**σ (S/m)**
Experiment		−210	1350
BoltzTrap-	CRTA	−255	2018
PERTURBO	τ_{e-ph}	−216	54096
	$\left(\tau_{e-ph}^{-1} + \tau_{ion}^{-1}\right)^{-1}$	−207	1400

In-plane thermal transport

Heat diffusion imaging was applied to a second sample of the same 25 nm thickness to extract the in-plane thermal conductivity. An optical image of the sample as well as a thermoreflectance map is provided in Fig. 4(a) and (b). The sample surface temperature drops exponentially as a function

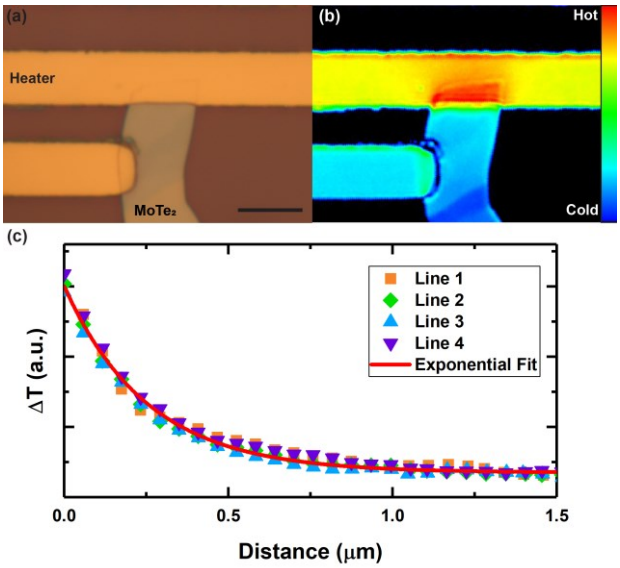

Fig. 4 (a) Optical image of the $MoTe_2$ device for thermal transport measurement. The scale bar is 5 μm. (b) Thermoreflectance map of the sample surface with 5 V supplied to the heater. Temperature decay curves were taken along the sample perpendicular to the heater. (c) Temperature decay curves and their corresponding exponential fit for thermal conductivity extraction.

of the distance away from the heater and can be fitted into a model for thermal conductivity extraction. Several example temperature decay curves along with an exponential fit are shown in Fig. 4(c). An in-plane thermal conductivity of 9.8 ± 3.7 $Wm^{-1}K^{-1}$ was obtained for $MoTe_2$ at room temperature. The error accounts for the variations from the multiple extracted temperature decay profiles for averaging. To the best of our knowledge, this thermal conductivity value is the first reported in multilayer $MoTe_2$ flakes. According to the Wiedemann-Franz law, the electronic contribution to the thermal conductivity is only on the order of 0.01 $Wm^{-1}K^{-1}$, which is negligible even with back gate modulation added. Therefore, we assume gating does not change the thermal conductivity.

Figure 5 shows the temperature dependence of the calculated thermal conductivity of $MoTe_2$ bulk along the in-plane direction from 200 K to 1000 K. The lattice thermal conductivity of $MoTe_2$ is calculated within both the relaxation time approximation (RTA) considering 3-phonon processes and the full iterative solution to the phonon Boltzmann equation for an isotopically pure sample. While the RTA results are closer to the experimentally measured value, it is known that the RTA solution gives a poor approximation to the lattice thermal conductivity compared to the full iterative method. These results are obtained by considering the interaction cutoff for cubic interatomic force constants calculations up to the seventh nearest neighbor. At room temperature, the calculated thermal conductivity of the isotopically pure bulk $MoTe_2$ is 24 $Wm^{-1}K^{-1}$ which is on the same order of magnitude but larger than our experimentally measured value of 9.8 ± 3.7 $Wm^{-1}K^{-1}$. The addition of the naturally occurring isotope scattering lowers the thermal conductivity by 10% to 22 W/mK. The measured sample is a flake with the thickness of 25 nm. The addition of size effect in the simplest approximation can be done by adding a v/L term, where v is the group velocity and L is the thickness, to the scattering rates to serve as the boundary scattering. The addition of this boundary scattering term lowers the thermal conductivity further by 22% and is shown in the plot by the green dashed line. This is still larger than the experimentally measured value. The difference can be attributed to defects inside the experimental sample as well as phonon-electron scattering rates.

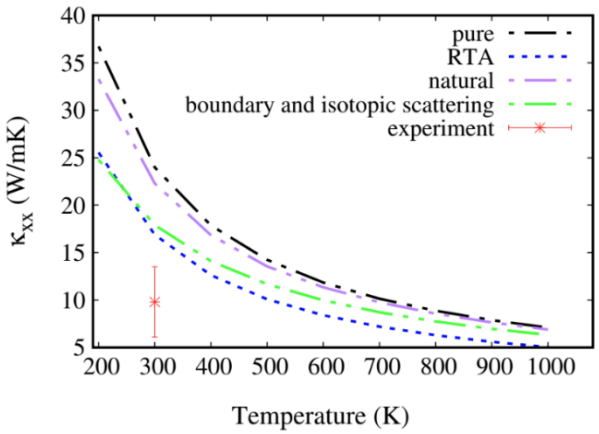

Fig. 5 Calculated thermal conductivity versus temperature of natural and pure $MoTe_2$ bulk along in-plane direction, and compared with experimental value.

Power factor and *ZT*

The peak power factor of thin $MoTe_2$ is expected to occur at the highest positive gate voltage since the improvement from the increasing electrical conductivity exceeds the impact from the decreasing Seebeck coefficient. By combining the experimental electrical conductivity and the theoretically predicted Seebeck coefficient, the peak *PFT* reaches 0.027 $Wm^{-1}K^{-1}$ at V_g = 80 V. Although our sample does not possess the highest electrical conductivity or the largest Seebeck coefficient value in comparison to the other two literature samples, by reaching a good balance between the two interrelated parameters, our peak *PFT* is comparable to the bulk single crystal $MoTe_2$ value[30] and is one order of magnitude larger than that of sputtered thin film $MoTe_2$ [31]. Compared to the value of 0.018 $Wm^{-1}K^{-1}$ at V_g = 0 V, the back gate modulation is able to enhance the *PFT* by 45%.

The peak *ZT* at room temperature is about 0.003. We expect the figure of merit to improve at higher temperatures, as was seen in the case of $MoTe_2$ thin films[31]. Its performance might be further improved via a few routes. For example, previous research has shown that hBN substrate is flatter and has fewer charge puddles compared to SiO_2, which can greatly improve the transport properties of 2D samples[6,13]. Estimation based on experimental conductivity and carrier concentration indicates

that the mobility of the sample was only 3 $cm^2V^{-1}s^{-1}$. Optimization of the fabrication process might produce samples with higher mobility.

Conclusions

In summary, we have exfoliated and fabricated 2H-MoTe2 samples for in-plane thermoelectric transport characterization. Back gate bias was applied to tune the Fermi level of the device and thus the electrical properties. The electrical conductivity increased with increasing gate voltages while the Seebeck coefficient values remained constant within the experimental error bar. The peak *PFT* of 0.027 $Wm^{-1}K^{-1}$ was obtained at the largest positive bias of +80 V, which was a 45% increase compared to the zero-bias value. These experimental results were supported by first-principles calculations which accounted for electron-phonon scattering and ionized impurity scattering. With an in-plane thermal conductivity of 9.8 ± 3.7 $Wm^{-1}K^{-1}$, the *ZT* of 2H-MoTe2 was estimated to be 0.003. The power factor and the ZT values will be larger at higher temperatures. The thermal conductivity can be manipulated and increased by 3.9 W/mK under a 1 K temperature difference, by applying an optimum electrical current and using the active cooling method. Further enhancement of the device performance might be achieved by increasing the temperature, using hBN as a substrate, and optimizing fabrication processes to increase carrier mobility. This study adds to the 2D thermoelectric database and is a solid first step in utilizing 2D 2H-$MoTe_2$ as a thermoelectric material.

Author Contributions

M.Z. supervised the project. T.Z. fabricated the devices and performed experimental characterizations. S.S.D. performed the electronic first-principles calculations. S.N. and K.E. performed the thermal conductivity calculations. S.K. and A.V.D. grew MoTe2 single crystals. C.C. helped with AFM measurements. T.Z., S.S.D., and M.Z. drafted the manuscript. All authors reviewed the manuscript prior to submission.

Conflicts of interest

There are no conflicts to declare.

Acknowledgements

T.Z., S.S.D., and M.Z. acknowledge the support by NSF, grant number 2230352. S. K. and A. V. D. acknowledge support through the Materials Genome Initiative funding allocated to the National Institute of Standards and Technology.

Disclaimer: Certain commercial equipment, instruments, or materials are identified in this paper in order to specify the experimental procedure adequately. Such identification is not intended to imply recommendation or endorsement by the National Institute of Standards and Technology, nor is it intended to imply that the materials or equipment identified are necessarily the best available for the purpose.

Notes and references

(1) Li, Q.; Hao, Q.; Zhu, T.; Zebarjadi, M.; Takahashi, K. Nanostructured and Heterostructured 2D Materials for Thermoelectrics. *Eng. Sci.* **2021**, *13*, 24–50. https://doi.org/10.30919/es8d1136.

(2) Pop, E. Energy Dissipation and Transport in Nanoscale Devices. *Nano Res.* **2010**, *3* (3), 147–169. https://doi.org/10.1007/s12274-010-1019-z.

(3) Akinwande, D.; Brennan, C. J.; Bunch, J. S.; Egberts, P.; Felts, J. R.; Gao, H.; Huang, R.; Kim, J.-S.; Li, T.; Li, Y.; Liechti, K. M.; Lu, N.; Park, H. S.; Reed, E. J.; Wang, P.; Yakobson, B. I.; Zhang, T.; Zhang, Y.-W.; Zhou, Y.; Zhu, Y. A Review on Mechanics and Mechanical Properties of 2D Materials—Graphene and Beyond. *Extrem. Mech. Lett.* **2017**, *13*, 42–77. https://doi.org/10.1016/j.eml.2017.01.008.

(4) Ares, P.; Novoselov, K. S. Recent Advances in Graphene and Other 2D Materials. *Nano Mater. Sci.* **2022**, *4* (1), 3–9. https://doi.org/10.1016/J.NANOMS.2021.05.002.

(5) Novoselov, K. S.; Geim, A. K.; Morozov, S. V.; Jiang, D.; Zhang, Y.; Dubonos, S. V.; Grigorieva, I. V.; Firsov, A. A. Electric Field Effect in Atomically Thin Carbon Films. *Science (80-.). 306* (5696), 666–669. https://doi.org/10.1126/science.1102896.

(6) Duan, J.; Wang, X.; Lai, X.; Li, G.; Watanabe, K.; Taniguchi, T.; Zebarjadi, M.; Andrei, E. Y. High Thermoelectricpower Factor in Graphene/HBN Devices. *Proc. Natl. Acad. Sci.* **2016**, *113* (50), 14272–14276. https://doi.org/10.1073/pnas.1615913113.

(7) Zebarjadi, M. Electronic Cooling Using Thermoelectric Devices. *Appl. Phys. Lett.* **2015**, *106* (20). https://doi.org/10.1063/1.4921457.

(8) Adams, M. J.; Verosky, M.; Zebarjadi, M.; Heremans, J. P. High Switching Ratio Variable-Temperature Solid-State Thermal Switch Based on Thermoelectric Effects. *Int. J. Heat Mass Transf.* **2019**, *134*, 114–118. https://doi.org/10.1016/J.IJHEATMASSTRANSFER.2018.12.154.

(9) Adams, M. J.; Verosky, M.; Zebarjadi, M.; Heremans, J. P. Active Peltier Coolers Based on Correlated and Magnon-Drag Metals. *Phys. Rev. Appl.* **2019**, *11* (5). https://doi.org/10.1103/PhysRevApplied.11.054008.

(10) Snyder, G. J.; Toberer, E. S. Complex Thermoelectric Materials. *Nat. Mater.* **2008**, *7* (2), 105–114. https://doi.org/10.1038/nmat2090.

(11) Markov, M.; Hu, X.; Liu, H.-C.; Liu, N.; Poon, S. J.; Esfarjani, K.; Zebarjadi, M. Semi-Metals as Potential Thermoelectric Materials. *Sci. Rep.* **2018**, *8* (1), 9876. https://doi.org/10.1038/s41598-018-28043-3.

(12) Hippalgaonkar, K.; Wang, Y.; Ye, Y.; Qiu, D. Y.; Zhu, H.; Wang, Y.; Moore, J.; Louie, S. G.; Zhang, X. High Thermoelectric Power Factor in Two-Dimensional Crystals of MoS2. *Phys. Rev. B* **2017**, *95* (11), 115407. https://doi.org/10.1103/PhysRevB.95.115407.

(13) Wu, J.; Liu, Y.; Liu, Y.; Cai, Y.; Zhao, Y.; Ng, H. K.; Watanabe, K.; Taniguchi, T.; Zhang, G.; Qiu, C.-W.; Chi, D.; Neto, A. H. C.; Thong, J. T. L.; Loh, K. P.; Hippalgaonkar, K. Large Enhancement of Thermoelectric Performance in MoS 2/h-BN Heterostructure Due to Vacancy-Induced Band Hybridization. *Proc. Natl. Acad. Sci.* **2020**, *117* (25), 13929–13936. https://doi.org/10.1073/pnas.2007495117.

(14) Wu, J.; Schmidt, H.; Amara, K. K.; Xu, X.; Eda, G.; Özyilmaz, B. Large Thermoelectricity via Variable Range Hopping in Chemical Vapor Deposition Grown Single-Layer MoS 2. *Nano Lett.* **2014**, *14* (5), 2730–2734. https://doi.org/10.1021/nl500666m.

(15) Kayyalha, M.; Maassen, J.; Lundstrom, M.; Shi, L.; Chen, Y. P. Gate-Tunable and Thickness-Dependent Electronic and Thermoelectric Transport in Few-Layer MoS2. *J. Appl. Phys.* **2016**, *120* (13), 134305. https://doi.org/10.1063/1.4963364.

(16) Yan, R.; Simpson, J. R.; Bertolazzi, S.; Brivio, J.; Watson, M.; Wu, X.; Kis, A.; Luo, T.; Hight Walker, A. R.; Xing, H. G. Thermal Conductivity of Monolayer Molybdenum Disulfide Obtained from Temperature-Dependent Raman Spectroscopy. *ACS Nano* **2014**, *8* (1), 986–993. https://doi.org/10.1021/nn405826k.

(17) Zhang, X.; Sun, D.; Li, Y.; Lee, G.-H.; Cui, X.; Chenet, D.; You, Y.; Heinz, T. F.; Hone, J. C. Measurement of Lateral and Interfacial Thermal Conductivity of Single- and Bilayer MoS 2 and MoSe 2 Using Refined Optothermal Raman Technique. *ACS Appl. Mater. Interfaces* **2015**, *7* (46), 25923–25929. https://doi.org/10.1021/acsami.5b08580.

(18) Rahman, M.; Shahzadeh, M.; Pisana, S. Simultaneous Measurement of Anisotropic Thermal Conductivity and Thermal Boundary Conductance of 2-Dimensional Materials. *J. Appl. Phys.* **2019**, *126* (20), 205103. https://doi.org/10.1063/1.5118315.

(19) Yarali, M.; Wu, X.; Gupta, T.; Ghoshal, D.; Xie, L.; Zhu, Z.; Brahmi, H.; Bao, J.; Chen, S.; Luo, T.; Koratkar, N.; Mavrokefalos, A. Effects of Defects on the Temperature-Dependent Thermal Conductivity of Suspended Monolayer Molybdenum Disulfide Grown by Chemical Vapor Deposition. *Adv. Funct. Mater.* **2017**, *27* (46), 1704357. https://doi.org/10.1002/adfm.201704357.

(20) Jo, I.; Pettes, M. T.; Ou, E.; Wu, W.; Shi, L. Basal-Plane Thermal Conductivity of Few-Layer Molybdenum Disulfide. *Appl. Phys. Lett.* **2014**, *104* (20), 201902. https://doi.org/10.1063/1.4876965.

(21) Zhao, Y.; Zheng, M.; Wu, J.; Huang, B.; Thong, J. T. L. Studying Thermal Transport in Suspended Monolayer Molybdenum Disulfide Prepared by a Nano-Manipulator-Assisted Transfer Method. *Nanotechnology* **2020**, *31* (22), 225702. https://doi.org/10.1088/1361-6528/ab7647.

(22) Gabourie, A. J.; Suryavanshi, S. V.; Farimani, A. B.; Pop, E. Reduced Thermal Conductivity of Supported and Encased Monolayer and Bilayer MoS 2. *2D Mater.* **2021**, *8* (1), 011001. https://doi.org/10.1088/2053-1583/aba4ed.

(23) Ruppert, C.; Aslan, B.; Heinz, T. F. Optical Properties and Band Gap of Single- and Few-Layer MoTe 2 Crystals. *Nano Lett.* **2014**, *14* (11), 6231–6236. https://doi.org/10.1021/nl502557g.

(24) Lezama, I. G.; Arora, A.; Ubaldini, A.; Barreteau, C.; Giannini, E.; Potemski, M.; Morpurgo, A. F. Indirect-to-Direct Band Gap Crossover in Few-Layer MoTe 2. *Nano Lett.* **2015**, *15* (4), 2336–2342. https://doi.org/10.1021/nl5045007.

(25) Yang, Y.; Zhu, X.; Zhang, K.; Zhu, H.; Chen, L.; Sun, Q. Observation of Different Transport Behaviors in a Two-Dimensional MoTe2 Field-Effect Transistor with Engineered Gate Stack. *Microelectron. Eng.* **2021**, *237*, 111497. https://doi.org/10.1016/j.mee.2020.111497.

(26) Gong, C.; Zhang, Y.; Chen, W.; Chu, J.; Lei, T.; Pu, J.; Dai, L.; Wu, C.; Cheng, Y.; Zhai, T.; Li, L.; Xiong, J. Electronic and Optoelectronic Applications Based on 2D Novel Anisotropic Transition Metal Dichalcogenides. *Adv. Sci.* **2017**, *4* (12), 1700231. https://doi.org/10.1002/advs.201700231.

(27) Lin, Y.-F.; Xu, Y.; Wang, S.-T.; Li, S.-L.; Yamamoto, M.; Aparecido-Ferreira, A.; Li, W.; Sun, H.; Nakaharai, S.; Jian, W.-B.; Ueno, K.; Tsukagoshi, K. Ambipolar MoTe 2 Transistors and Their Applications in Logic Circuits. *Adv. Mater.* **2014**, *26* (20), 3263–3269. https://doi.org/10.1002/adma.201305845.

(28) Chang, Y.-M.; Lin, C.-Y.; Lin, Y.-F.; Tsukagoshi, K. Two-Dimensional MoTe 2 Materials: From Synthesis, Identification, and Charge Transport to Electronics Applications. *Jpn. J. Appl. Phys.* **2016**, *55* (11), 1102A1. https://doi.org/10.7567/JJAP.55.1102A1.

(29) Bie, Y.-Q.; Grosso, G.; Heuck, M.; Furchi, M. M.; Cao, Y.; Zheng, J.; Bunandar, D.; Navarro-Moratalla, E.; Zhou, L.; Efetov, D. K.; Taniguchi, T.; Watanabe, K.; Kong, J.; Englund, D.; Jarillo-Herrero, P. A MoTe2-Based Light-Emitting Diode and Photodetector for Silicon Photonic Integrated Circuits. *Nat. Nanotechnol.* **2017**, *12* (12), 1124–1129. https://doi.org/10.1038/nnano.2017.209.

(30) Conan, A.; Delaunay, D.; Bonnet, A.; Moustafa, A. G.; Spiesser, M. Temperature Dependence of the Electrical Conductivity and Thermoelectric Power in MoTe2 Single Crystals. *Phys. Status Solidi* **1979**, *94* (1), 279–286. https://doi.org/10.1002/pssb.2220940132.

(31) Shi, D.; Wang, G.; Li, C.; Shen, X.; Nie, Q. Preparation and Thermoelectric Properties of MoTe 2 Thin Films by Magnetron Co-Sputtering. *Vacuum* **2017**, *138*, 101–104. https://doi.org/10.1016/j.vacuum.2017.01.030.

(32) Yan, X.-J.; Lv, Y.-Y.; Li, L.; Li, X.; Yao, S.-H.; Chen, Y.-B.; Liu, X.-P.; Lu, H.; Lu, M.-H.; Chen, Y.-F. Investigation on the Phase-Transition-Induced Hysteresis in the Thermal Transport along the c-Axis of MoTe2. *npj Quantum Mater.* **2017**, *2* (1), 31. https://doi.org/10.1038/s41535-017-0031-x.

(33) Shafique, A.; Shin, Y. H. Strain Engineering of Phonon Thermal Transport Properties in Monolayer 2H-MoTe2. *Phys. Chem. Chem. Phys.* **2017**, *19* (47), 32072–32078. https://doi.org/10.1039/C7CP06065C.

(34) Addou, R.; Smyth, C. M.; Noh, J.-Y.; Lin, Y.-C.; Pan, Y.; Eichfeld, S. M.; Fölsch, S.; Robinson, J. A.; Cho, K.; Feenstra, R. M.; Wallace, R. M. One Dimensional Metallic Edges in Atomically Thin WSe 2 Induced by Air Exposure. *2D Mater.*

2018, *5* (2), 025017. https://doi.org/10.1088/2053-1583/aab0cd.

(35) Zhu, T.; Olson, D. H.; Hopkins, P. E.; Zebarjadi, M. Heat Diffusion Imaging: In-Plane Thermal Conductivity Measurement of Thin Films in a Broad Temperature Range. *Rev. Sci. Instrum.* **2020**, *91* (11), 113701. https://doi.org/10.1063/5.0024476.

(36) Giannozzi, P.; Baroni, S.; Bonini, N.; Calandra, M.; Car, R.; Cavazzoni, C.; Ceresoli, D.; Chiarotti, G. L.; Cococcioni, M.; Dabo, I.; Dal Corso, A.; de Gironcoli, S.; Fabris, S.; Fratesi, G.; Gebauer, R.; Gerstmann, U.; Gougoussis, C.; Kokalj, A.; Lazzeri, M.; Martin-Samos, L.; Marzari, N.; Mauri, F.; Mazzarello, R.; Paolini, S.; Pasquarello, A.; Paulatto, L.; Sbraccia, C.; Scandolo, S.; Sclauzero, G.; Seitsonen, A. P.; Smogunov, A.; Umari, P.; Wentzcovitch, R. M. QUANTUM ESPRESSO: A Modular and Open-Source Software Project for Quantum Simulations of Materials. *J. Phys. Condens. Matter* **2009**, *21* (39), 395502. https://doi.org/10.1088/0953-8984/21/39/395502.

(37) Vanderbilt, D. Soft Self-Consistent Pseudopotentials in a Generalized Eigenvalue Formalism. *Phys. Rev. B* **1990**, *41* (11), 7892–7895. https://doi.org/10.1103/PhysRevB.41.7892.

(38) Perdew, J. P.; Ruzsinszky, A.; Csonka, G. I.; Vydrov, O. A.; Scuseria, G. E.; Constantin, L. A.; Zhou, X.; Burke, K. Restoring the Density-Gradient Expansion for Exchange in Solids and Surfaces. *Phys. Rev. Lett.* **2008**, *100* (13), 136406. https://doi.org/10.1103/PhysRevLett.100.136406.

(39) Wilson, J. A.; Yoffe, A. D. The Transition Metal Dichalcogenides Discussion and Interpretation of the Observed Optical, Electrical and Structural Properties. *Adv. Phys.* **1969**, *18* (73). https://doi.org/10.1080/00018736900101307.

(40) Zhou, J.-J.; Park, J.; Lu, I.-T.; Maliyov, I.; Tong, X.; Bernardi, M. Perturbo: A Software Package for Ab Initio Electron–Phonon Interactions, Charge Transport and Ultrafast Dynamics. *Comput. Phys. Commun.* **2021**, *264*, 107970. https://doi.org/10.1016/j.cpc.2021.107970.

(41) Lundstrom, M. Fundamentals of Carrier Transport, 2nd Edn. *Meas. Sci. Technol.* **2002**, *13* (2), 230–230. https://doi.org/10.1088/0957-0233/13/2/703.

(42) Marzari, N.; Mostofi, A. A.; Yates, J. R.; Souza, I.; Vanderbilt, D. Maximally Localized Wannier Functions: Theory and Applications. *Rev. Mod. Phys.* **2012**, *84* (4), 1419–1475. https://doi.org/10.1103/RevModPhys.84.1419.

(43) Giustino, F.; Cohen, M. L.; Louie, S. G. Electron-Phonon Interaction Using Wannier Functions. *Phys. Rev. B* **2007**, *76* (16), 165108. https://doi.org/10.1103/PhysRevB.76.165108.

(44) Liu, J.; Wang, Y.; Xiao, X.; Zhang, K.; Guo, N.; Jia, Y.; Zhou, S.; Wu, Y.; Li, Q.; Xiao, L. Conversion of Multi-Layered MoTe2 Transistor Between P-Type and N-Type and Their Use in Inverter. *Nanoscale Res. Lett.* **2018**, *13* (1), 291. https://doi.org/10.1186/s11671-018-2721-0.

(45) Madsen, G. K. H.; Singh, D. J. BoltzTraP. A Code for Calculating Band-Structure Dependent Quantities. *Comput. Phys. Commun.* **2006**, *175* (1), 67–71. https://doi.org/10.1016/j.cpc.2006.03.007.

(46) Nag, B. R. *Electron Transport in Compound Semiconductors*; Nag, B., Ed.; Springer Series in Solid-State Sciences; Springer Berlin Heidelberg: Berlin, Heidelberg, 1980; Vol. 11. https://doi.org/10.1007/978-3-642-81416-7.

(47) Rosul, M. G.; Zebarjadi, M. Effect of Electron-Phonon Interaction and Ionized Impurity Scattering on the Room-Temperature Thermoelectric Properties of Bulk MoSe2. *J. Phys. Chem. C* **2022**, *126* (35), 15011–15018. https://doi.org/10.1021/acs.jpcc.2c03782.

(48) Das, S.; Rosul, G.; Zebarjadi, M. Optimization of the Thermoelectric Properties of SnSe2 Using First-Principles Calculations. *J. Phys. Chem. C* **2023**, *127*.

(49) Fletcher, R.; Pudalov, V. M.; Radcliffe, A. D. B.; Possanzini, C. Critical Behaviour of Thermopower and Conductivity at the Metal-Insulator Transition in High-Mobility Si-MOSFETs. *Semicond. Sci. Technol.* **2001**, *16* (5), 386–393. https://doi.org/10.1088/0268-1242/16/5/318.

(50) Yun, W. S.; Han, S. W.; Hong, S. C.; Kim, I. G.; Lee, J. D. Thickness and Strain Effects on Electronic Structures of Transition Metal Dichalcogenides: 2H- <math Display="inline"> <mrow> <mi>M</Mi> <msub> <mi>X</Mi> <mn>2</Mn> </Msub> </Mrow> </Math> Semiconductors (<math Display="inline"> <mi>M</Mi> </Math> <math. *Phys. Rev. B* **2012**, *85* (3), 033305. https://doi.org/10.1103/PhysRevB.85.033305.

(51) Reshak, A. H.; Auluck, S. Band Structure and Optical Response of <math Display="inline"> <mrow> <mn>2</Mn> <mi>H</Mi> <mtext>−</Mtext> <mi Mathvariant="normal">Mo</Mi> <msub> <mi>X</Mi> <mn>2</Mn> </Msub> </Mrow> </Math> Compounds (<math Display="inline"> <mrow> <mi>X</Mi> <mo>=<. *Phys. Rev. B* **2005**, *71* (15), 155114. https://doi.org/10.1103/PhysRevB.71.155114.

(52) Froehlicher, G.; Lorchat, E.; Berciaud, S. Direct versus Indirect Band Gap Emission and Exciton-Exciton Annihilation in Atomically Thin Molybdenum Ditelluride MoTe2. *Phys. Rev. B* **2016**, *94* (8), 085429. https://doi.org/10.1103/PhysRevB.94.085429.

(53) Pike, N. A.; Dewandre, A.; Van Troeye, B.; Gonze, X.; Verstraete, M. J. Vibrational and Dielectric Properties of the Bulk Transition Metal Dichalcogenides. *Phys. Rev. Mater.* **2018**, *2* (6), 063608. https://doi.org/10.1103/PhysRevMaterials.2.063608.

(54) Nag, B. R. *Electron Transport in Compound Semiconductors*; Springer Science & Business Media, 2012; Vol. 11.